Research Article

Graphitic carbon nitride nanoplatelets incorporated titania based type-II heterostructure and its enhanced performance in photoelectrocatalytic water splitting

P. Mary Rajaitha[1] · K. Shamsa[1] · C. Murugan[1,2] · K. B. Bhojanaa[1,2] · S. Ravichandran[2,3] · K. Jothivenkatachalam[4] · A. Pandikumar[1,2]

Abstract

In this present work, the synthesis of $g\text{-}C_3N_4/TiO_2$ nanocomposites with different wt.% $g\text{-}C_3N_4$ to form a type-II heterostructure and its potential application towards photoelectrocatalytic water splitting was discussed. The synthesized $g\text{-}C_3N_4$ nanoplatelets incorporated TiO_2 nanocomposites were characterized by various analytical techniques such as UV–vis diffuse reflectance spectroscopy, X-ray diffraction, Fourier transform infrared spectroscopy, photoluminescence spectroscopy, X-ray photoelectron spectroscopy, thermogravimetric analysis and high-resolution transmission electron microscopy (HRTEM). HRTEM confirms the formation of type-II heterostructure consists of $g\text{-}C_3N_4$ nanoplatelets incorporated titania in the nanocomposite. The photoelectrocatalytic activity of the TiO_2, $g\text{-}C_3N_4$, and $g\text{-}C_3N_4/TiO_2$ nanocomposite were investigated under AM 1.5G (100 mW cm^{-2}) illumination in 1 M KOH. The $g\text{-}C_3N_4/TiO_2$ (with 10 wt.% of $g\text{-}C_3N_4$) nanocomposite photoanode exhibits photocurrent density of 142.7 µA cm^{-2} (at 1.23 V vs. RHE) which is ~ 1.8-fold higher than bare TiO_2 (80.5 µA cm^{-2} at 1.23 V vs. RHE). The enhancement in PEC activity explained by formation of type-II heterostructure between $g\text{-}C_3N_4$ and TiO_2, which reduced the recombination rate of photo-generated electron–hole pairs and also extends the absorption of TiO_2 to visible light range and boost up the interfacial charge transfer between electrode/electrolyte interface, which enhance the PEC activity of the $g\text{-}C_3N_4/TiO_2$ nanocomposite towards water splitting.

Keywords Titanium dioxide · Graphitic carbon nitride · Nanoplatelets · Type-II heterostructure · Photoelectrocatalysis · Water splitting

1 Introduction

Energy crises and environmental pollution has become a key problem due to continuous increase in world population. World primary energy supply is fossil fuel, use of these leads to the emission of greenhouse gas including carbon dioxide. The over use of fossil fuel has intensified the energy crises and environmental pollution, due to which the need to find an alternative energy source arises

[1, 2]. The development of sustainable and renewable energy source is an essential requirement. An ideal way to solve the energy crises is generation of hydrogen utilizing solar energy, since the solar energy is an inexhaustible and clean resource [3–6]. The conventional fossil fuel is expected to be replaced by solar energy in near future. Among different solar energy harvesting application, water splitting using solar energy is widely studied [7–10].

✉ A. Pandikumar, pandikumarinbox@gmail.com; pandikumar@cecri.res.in | [1]Functional Materials Division, CSIR-Central Electrochemical Research Institute, Karaikudi, Tamil Nadu 630 003, India. [2]Academy of Scientific and Innovative Research (AcSIR), Ghaziabad 201002, India. [3]Electro-Inorganic Chemicals Division, CSIR-Central Electrochemical Research Institute, Karaikudi, Tamil Nadu 630 003, India. [4]Department of Chemistry, Anna University, BIT Campus, Tiruchirappalli, Tamilnadu 620024, India.

To overcome the issues caused by using non-renewable energy sources, production of hydrogen from renewable energy sources opened up a new path to get clean and storable energy. The energy from water and solar light can be harvested by using a photoelectrochemical (PEC) cell. The photoelectrode used in the PEC cells must have some prime requirement, an optimal band gap energy of 2 eV, more negative conduction band potential compare to hydrogen reaction potential, enough negative flat band potential and chemical stability against photo-corrosion in an aqueous environment [11, 12]. As a result, the development of photoelectrode has gained a considerable attention and many semiconductors like ZnO, WO_3, V_2O_5, Fe_2O_3, etc. have been studied. But their industrial application is limited due to its high cost and poor stability towards photooxidation.

Titanium dioxide is a semiconductor metal oxide that has been studied widely because of its low cost, non-toxic and excellent photochemical and chemical stability. Also, it has good catalytic activity, abundant in nature, able to resist photocorrosion and hence finds application in photocatalytic and photoelectrocatalytic fields. [13, 14]. It has a band gap of 3.0–3.2 eV and can be excited only in UV region which accounts for about only 4% of solar spectrum, it does not respond to visible light [15, 16]. The overall performance is limited by the photo-excited charges trapped within the TiO_2 network and the recombination of the electron hole pair. Various methods have been employed to address these issues like elemental doping [17], combining with suitable semiconductors [18] and loading with noble metal as co-catalysts [19]. TiO_2 is also integrated with conductive carbonaceous material to improve its photocatalytic and photoelectrochemical activity [20].

Recently, researchers are focusing on the metal-free semiconducting material, graphitic carbon nitride (g-C_3N_4) due to its structure and physicochemical properties. It has good chemical and thermal stability with bandgap of 2.7 eV. It has a high stability in acidic and alkaline electrolyte due to its strong covalent bond between carbon and nitrogen atoms, which is favorable for PEC application [21–23]. However, its photocatalytic activity is reduced due its low quantum efficiency and high electron hole pair recombination. In order to increase the performance of g-C_3N_4 many strategies have been employed like non-metal doping [24], preparation of mesoporous C_3N_4 [25] and formation of heterostructure between C_3N_4 and other metals [26].

Structures like nanobelts [27], nanosheets [28] and nanoplates [29] which has a 2D structure has been noted as an excellent material for photochemical water splitting due to improved charge separation and higher percentage of surface electron. Cheng et al. [30] reported a mild

alkali treatment route for the synthesis of carbon nitride colloid. Yan et al. [31] reported the synthesis of ultrathin g-C_3N_4 nanosheets by exfoliation in hot water. Niu et al. [32] reported the synthesis of g-C_3N_4 by thermal etching process, but this is ended up with low efficiency. Yang et al. [33] reported the fabrication of g-C_3N_4 nanosheets by exfoliation of commercially available g-C_3N_4 powder in various solvents via sonication. Also, Zhang et al. [34] reported the exfoliation of g-C_3N_4 in water by using ultra-sonication. However, the sonochemical delamination method in organic solvents or water suffers from the long ultrasonic period and low exfoliation efficiency. Qian et al. [35] reported the process of exfoliation of graphitic carbon nitride by using ultrasonication assisted with graphene quantum dots. F. Cheng et al. reported the large-scale synthesis of stable colloid of g-C_3N_4 nanosheets was via a H_2SO_4 exfoliation route. This facilitates the fabrication of heterostructure by an electrostatic re-assembly between g-C_3N_4 nanosheets and various charged guests in different pH systems [36]. These 2D structure have a vast numbers of active edge sites which acts as an efficient catalytic center with high catalytic activity [32]. 2D g-C_3N_4 sheet can be delaminated from bulk g-C_3N_4 through thermal oxidation etching under heating at 500 °C in air. The photocatalytic activity of these g-C_3N_4 nanosheet was notably higher than bulk g-C_3N_4 because of its feasibility in tuning the band structure and improved charge separation [37].

To gain the advantages of both g-C_3N_4 and TiO_2 properties, in the present work, different weight percentages of g-C_3N_4 nanoplatelets incorporated with TiO_2 have synthesized and was characterized by UV–vis diffuse reflectance spectroscopy (UV–vis DRS), X-ray diffraction (XRD), X-ray photoelectron spectroscopy (XPS) and high resolution transmission electron microscopy (HRTEM). The photoelectrocatalytic materials (TiO_2, g-C_3N_4, and g-C_3N_4/TiO_2) performances were investigated towards water splitting under AM 1.5G (100 mW cm^{-2}) illumination in 1 M KOH. The g-C_3N_4/TiO_2 photoanode with 10 wt.% of g-C_3N_4 shows higher photoelectrocatalytic water splitting performance, which is two folds higher than that of the bare TiO_2.

2 Experimental methods

2.1 Chemicals and reagents

Chemicals such as melamine ($C_3H_6N_6$) and ammonium sulphate ($(NH_4)_2SO_4$) were purchased from Alfa Aesar, titanium dioxide (P-25-TiO_2) was procured from Acros Organics. All reagents were and used as received. Deionized water was used throughout the experiment which is collected from Millipore water system.

2.2 Preparation of graphitic carbon nitride

The g-C_3N_4 was prepared as follows (Fig. 1a). Initially, melamine and ammonium sulphate were taken in equal weight ratio and mixed thoroughly using an agate mortar and pestle for an hour. Here, ammonium sulphate was added as a chemical blowing agent, which could enhance the formation of g-C_3N_4 nanosheets [38, 39]. The resultant material was subjected to calcination at 550 °C with the ramp rate of 2 °C per min. After reaching 550 °C, it was kept at the same temperature for 2 h and naturally cooled down to room temperature.

2.3 Preparation of g-C_3N_4/TiO_2

The g-C_3N_4/TiO_2 nanocomposites were prepared as follows (Fig. 1b). Initially, an appropriate amount of g-C_3N_4 is dispersed in 1M H_2SO_4 and sonicated for 30 min. To the above mixture, 1 g of TiO_2 (P 25) was added under sonication for 10 min. The prepared solution was allowed to stir at 80 °C for 1 h. The pH of the solution was found to be 1. Then, ammonia was added to the above mixture till the pH reached 7 and it was allowed to stir for 30 min. The addition of H_2SO_4 into g-C_3N_4 NS helps in exfoliation of nanosheets, by bearing the positive charges and is further neutralized by adding ammonia [33, 40]. The final product was centrifuged, washed and dried. The 5, 10, 15, 20 and 25% weight percentages of g-C_3N_4/TiO_2 nanocomposites were prepared by the above said procedure and were denoted as 5% g-C_3N_4/TiO_2, 10% g-C_3N_4/TiO_2, 15% g-C_3N_4/TiO_2, 20% g-C_3N_4/TiO_2 and 25% g-C_3N_4/TiO_2 respectively.

2.4 Characterization techniques

The absorption features of all the synthesized samples were measured spectroscopically in diffuse reflectance mode with a UV–visible spectrophotometer (Varian, model: Cary 500 Scan). X-ray diffraction (XRD) patterns were characterized with Bruker AXS D8 Advance with Cu Kα radiation (λ = 1.54178 Å). Fourier transform infrared (FTIR) spectra were recorded by employing potassium bromide (KBr) disks using a Bruker Optik GmbH, Germany (Model: TENSOR 27) spectrometer. The photoluminescence (PL) spectra were characterized at room temperature by using F-7000 FL, Hitachi fluorescence spectrophotometer with an excitation wavelength of 370 nm. Thermogravimetric analysis (TGA) was characterized in TGA/DTA analyzer (SDT Q 600) in nitrogen atmosphere. Surface elemental analysis and oxidation state of sample was performed using X-ray photoelectron spectroscopy (XPS) with Mg Kα (1253.6 eV) as X-ray source (Thermo Scientific, MULTILAB 2000). The morphology was studied by using high resolution transmission electron microscopy (HRTEM) (200 kV, Tecnai G2 TF20).

2.5 Photoelectrochemical measurements

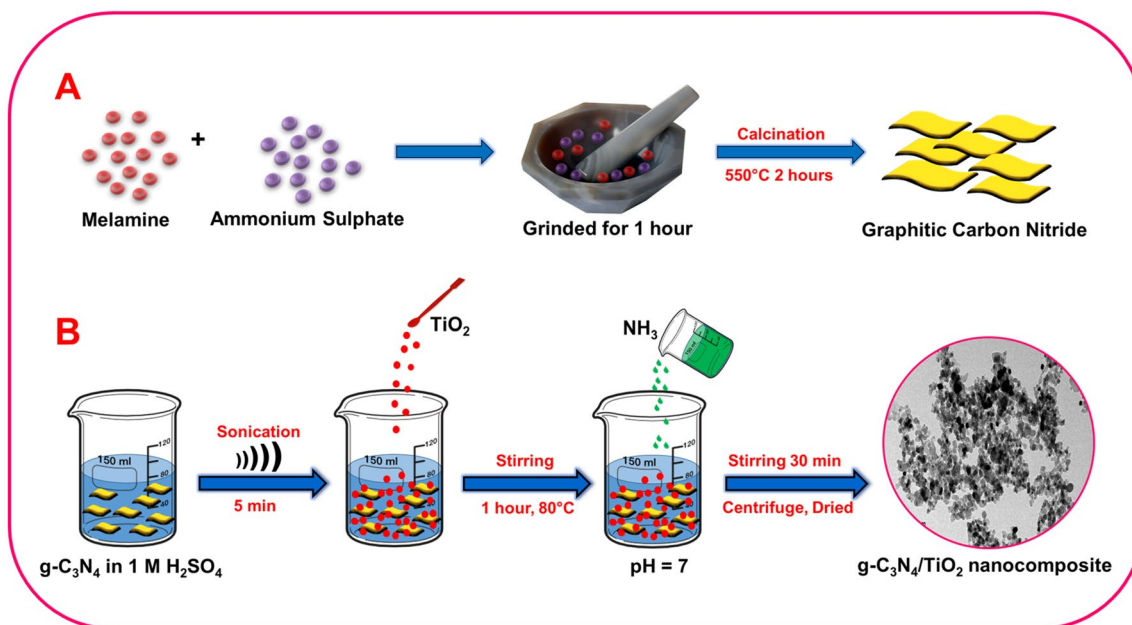The PEC water splitting experiment were done in 1 M KOH (pH = 13.2) electrolyte. Photocurrent was measured in a

Fig. 1 Synthetic scheme for the preparation of **a** g-C_3N_4 and **b** g-C_3N_4/TiO_2 nanocomposites

standard three-electrode configuration by using Origalys electrochemical workstation, the counter electrode is platinum, reference electrode is mercury–mercury oxide (Hg/HgO) and working electrode is prepared sample coated thin film. The synthesized samples were coated on the conducting side of FTO by doctor blade method. For coating, 10 mg of the synthesized sample is mixed with few drops of acetyl acetone and one drop of triton X 100 in a mortar. The ORIEL LCS-100 (Newport, USA) solar simulator with AM 1.5G (100 mW cm^{-2}) filter was employed as light source. The photocurrent response and electrochemical impedance spectroscopy (EIS) were measured at room temperature. All of the measured potentials were converted with respect to the reversible hydrogen electrode (RHE) using Eq. (1) with measured pH of electrolyte.

$$E_{RHE} = E_{(Hg/HgO)} + 0.0591 \times pH + E^o_{(Hg/HgO)} \qquad (1)$$

where E_{RHE} is the converted potential versus RHE, $E^o_{Hg/HgO} = 0.098$ V at 25 °C, pH and $E_{Hg/HgO}$ is the experimentally measured potential against Hg/HgO Ref. [41].

3 Results and discussion

3.1 Absorption studies

The optical property of TiO$_2$, g-C$_3$N$_4$ and g-C$_3$N$_4$/TiO$_2$ nanocomposites was studied by diffuse reflectance spectra (DRS) (Fig. 2).

In Fig. 2a, the absorption edge of TiO$_2$ was found at 410 nm, which belongs to UV region and unlikely to absorb in visible light. The g-C$_3$N$_4$ had an absorption edge at 460 nm and it has an intensive absorption in visible light region. The presence of g-C$_3$N$_4$ in the nanocomposites influences the TiO$_2$ absorption into visible light absorption. Figure 2b shows the DRS of g-C$_3$N$_4$/TiO$_2$ with different wt.% of g-C$_3$N$_4$. After increasing the wt.% of g-C$_3$N$_4$ in g-C$_3$N$_4$/TiO$_2$ nanocomposite, red shift was observed, the absorption of g-C$_3$N$_4$/TiO$_2$ shifted to longer wavelength region. The additional visible light absorption of the nanocomposite is due to the presence of g-C$_3$N$_4$ and the intensity of absorption increases with raise in g-C$_3$N$_4$ content [42, 43]. The absorption edge of g-C$_3$N$_4$/TiO$_2$ found in between g-C$_3$N$_4$ and TiO$_2$, indicates the existence of electronic interaction between g-C$_3$N$_4$ and TiO$_2$, it is favorable for photogenerated charge carrier transfer [44]. Figure 2c–e shows g-C$_3$N$_4$, TiO$_2$ and 10% g-C$_3$N$_4$/TiO$_2$, Plots of (αhυ)$^{1/2}$ versus hυ (eV) obtained for g-C$_3$N$_4$/TiO$_2$ with different wt.% of g-C$_3$N$_4$, Plot of band gap versus wt.% g-C$_3$N$_4$ in the g-C$_3$N$_4$/TiO$_2$ nanocomposite materials respectively.

The band gap energy of the obtained materials was calculated by using the Tacu's plot as shown below.

$$\alpha h\nu = A(h\nu - E_g)^2 \qquad (2)$$

where α is the absorption coefficient, h is the Planck's constant, ν is the light frequency, E_g is the band gap and A is a constant [44–48]. The band gap energies of TiO$_2$ and g-C$_3$N$_4$ was found to be 3.1 eV and 2.75 eV were found from the intercept of the tangent from the plot hυ (eV) versus (αhυ)$^{1/2}$. The band gap energy values were influenced by the g-C$_3$N$_4$ present in the nanocomposites. The band gap energies of the g-C$_3$N$_4$/TiO$_2$ nanocomposites with 5, 10, 15, 20 and 25 wt.% of g-C$_3$N$_4$ were found to be 2.82, 2.87, 2.77, 2.77 and 2.73 eV respectively. It is clearly observed that, the band gap energies were decreased gradually, as the weight of g-C$_3$N$_4$ increased as the weight of g-C$_3$N$_4$ increased in nanocomposite. This is mainly attributed to the formation of heterostructure between g-C$_3$N$_4$ and TiO$_2$ in the nanocomposite materials.

3.2 X-ray diffraction studies

X-ray diffraction was used to study the crystalline phase structure of the prepared nanocomposite materials. Figure 3a shows the XRD patterns obtained for g-C$_3$N$_4$, TiO$_2$ and 10% g-C$_3$N$_4$/TiO$_2$; Whereas Fig. 3b shows the XRD patterns obtained for g-C$_3$N$_4$/TiO$_2$ with different wt.% of g-C$_3$N$_4$. The samples displayed a good crystallinity. There was no appreciable change was observed, in the XRD patterns of pure TiO$_2$ and g-C$_3$N$_4$/TiO$_2$ nanocomposites. TiO$_2$ shows three major peaks at 25.51°, 48.1° and 37.97° due to the planes (101), (200) and (004). The strongest peak observed at 25.51° lies in the plane (101) due to the predominant presence of anatase phase in TiO$_2$. The g-C$_3$N$_4$ showed two major peaks at 27.43° corresponds to (002) plane and 13.03° corresponds to (100) plane due to stacking of conjugated aromatic system and due to the in-plane structural packing motif of tri-s-triazine units respectively. The (002) plane of g-C$_3$N$_4$ is overlapped with (110) plane of TiO$_2$ in the nanocomposite. Diffraction peaks matches well with the reported data (JCPDS 01-087-1526). Even after the addition of g-C$_3$N$_4$ up to 25 wt.%, the anatase and rutile peaks of TiO$_2$ in g-C$_3$N$_4$/TiO$_2$ nanocomposites is undisturbed (Fig. 3b).

3.3 FT-IR studies

The FT-IR spectra of the synthesized samples were investigated to study the interaction of TiO$_2$ and g-C$_3$N$_4$ in the prepared g-C$_3$N$_4$/TiO$_2$ nanocomposites. Figure 4 shows the FT-IR spectra obtained for (A) g-C$_3$N$_4$, TiO$_2$ and 10% g-C$_3$N$_4$/TiO$_2$ and (B) g-C$_3$N$_4$/TiO$_2$ with different wt.% of g-C$_3$N$_4$. The FT-IR spectrum of TiO$_2$ exhibits a band at 400–700 cm^{-1},
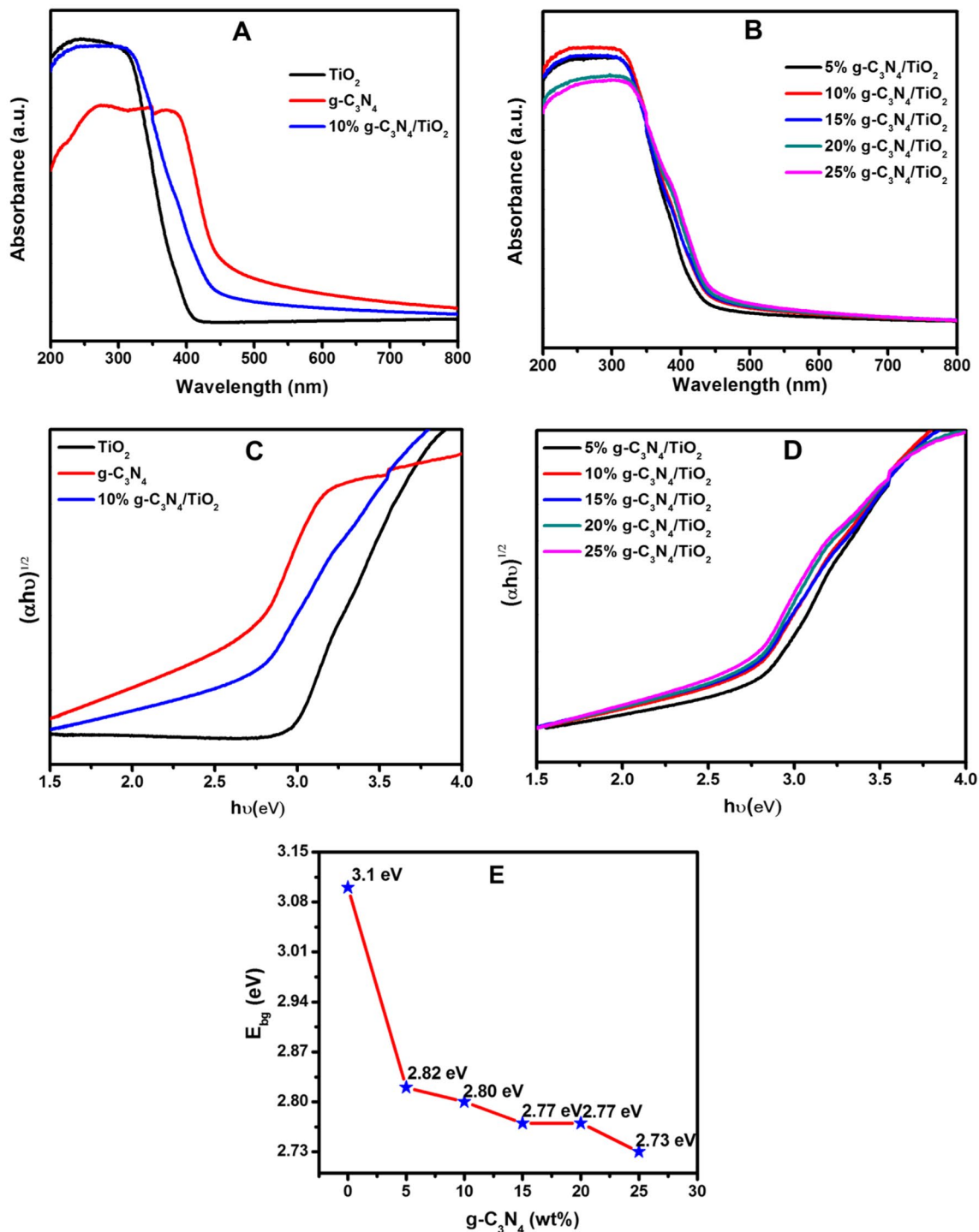
Fig. 2 Diffuse reflectance spectra obtained for **a** g-C$_3$N$_4$, TiO$_2$ and 10% g-C$_3$N$_4$/TiO$_2$. **b** Diffuse reflectance spectra of g-C$_3$N$_4$/TiO$_2$ with different wt.% of g-C$_3$N$_4$. Plots of (αhυ)$^{1/2}$ versus hυ (eV) obtained for **c** g-C$_3$N$_4$, TiO$_2$ and 10% g-C$_3$N$_4$/TiO$_2$. **d** Plots of (αhυ)$^{1/2}$ versus hυ (eV) obtained for g-C$_3$N$_4$/TiO$_2$ with different wt.% of g-C$_3$N$_4$. **e** Plot of band gap versus wt.% g-C$_3$N$_4$ in the g-C$_3$N$_4$/TiO$_2$ nanocomposite materials
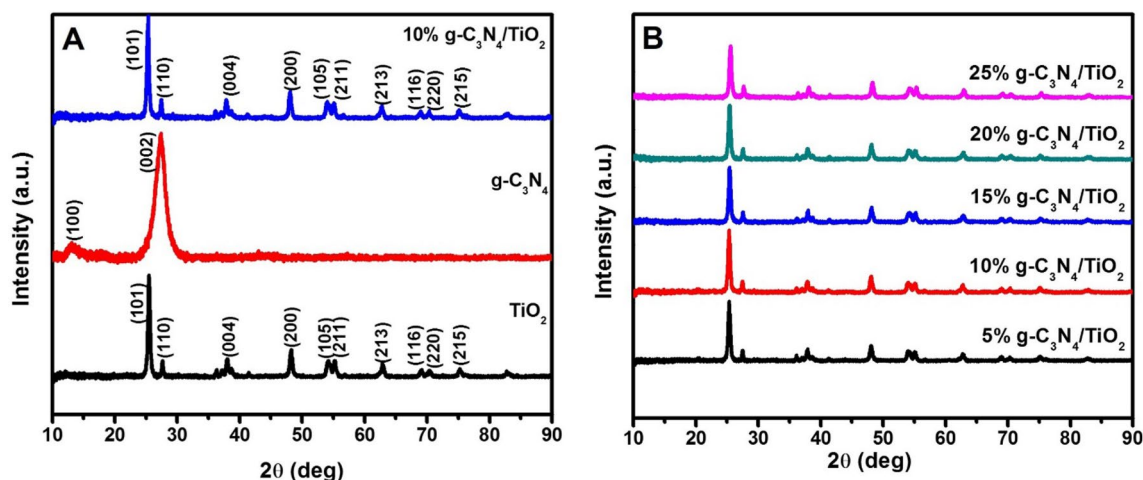
Fig. 3 XRD patterns obtained for **a** g-C$_3$N$_4$, TiO$_2$ and 10% g-C$_3$N$_4$/TiO$_2$, **b** g-C$_3$N$_4$/TiO$_2$ with different wt.% of g-C$_3$N$_4$
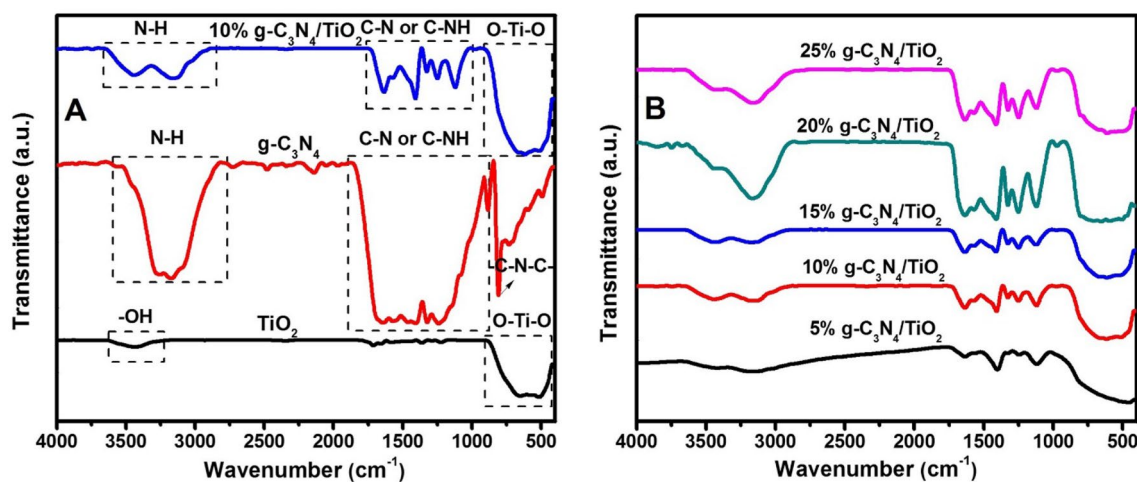
Fig. 4 FT-IR spectra obtained for **a** g-C$_3$N$_4$, TiO$_2$ and 10% g-C$_3$N$_4$/TiO$_2$ and **b** g-C$_3$N$_4$/TiO$_2$ with different wt.% of g-C$_3$N$_4$

is due to Ti–O–Ti stretching vibration and a weak band at 3400 cm^{-1} corresponds to –OH stretching vibration [49].

The peaks observed in the region of 1200–1650 cm^{-1} in the FT-IR spectra of g-C$_3$N$_4$ corresponds to the stretching and rotational vibration of C–N and C–NH bonds. The broad band observed at 2900–3600 cm^{-1} corresponds to stretching modes of the NH group. A sharp peak at 820 cm^{-1} is due to the bending vibration of heptazine rings [43]. The FT-IR spectra of the g-C$_3$N$_4$/TiO$_2$ composites with different wt.% of g-C$_3$N$_4$ exhibits all the main characteristic peaks of g-C$_3$N$_4$ and TiO$_2$ indicating the presence of g-C$_3$N$_4$ and TiO$_2$ in the composites.

3.4 Photoluminescence studies

The recombination process of photogenerated electron–hole pairs, was studied by photoluminescence spectra. Figure 5a shows the photoluminescence spectra of g-C$_3$N$_4$, TiO$_2$ and g-C$_3$N$_4$/TiO$_2$ nanocomposite with the excitation wavelength of 370 nm. A lower rate of recombination of photogenerated electron–hole pair gives a low PL intensity [50]. The pure TiO$_2$ had a weak intense PL band at 450 nm, which is due to the recombination of photoinduced electron and hole via oxygen vacancies. A strong PL band at 457 nm for pure g-C$_3$N$_4$ is due to high photoinduced electron recombination. The g-C$_3$N$_4$/TiO$_2$ nanocomposite exhibits a PL spectrum at 450 nm. It can be corresponded to the formation of heterostructures which leads to the photoinduced electron transfer from more negative conduction band of g-C$_3$N$_4$ to the conduction band of TiO$_2$ [42].
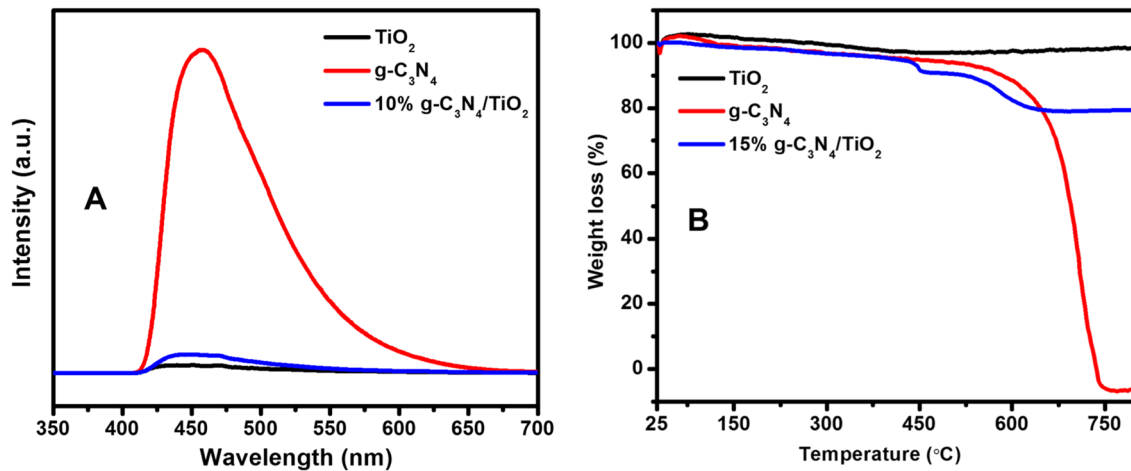
Fig. 5 a Photoluminescence spectra of g-C_3N_4, TiO_2 and 10%-g-C_3N_4/TiO_2 nanocomposite with the excitation wavelength of 370 nm, **b** TGA curves obtained for the g-C_3N_4, TiO_2 and 20%

g-C_3N_4/TiO_2 under nitrogen atmosphere from room temperature to 800 °C at a heating rate of 10 °C min^{-1}

3.5 XPS analysis

Figure 6a shows the XPS survey scan spectrum of g-C_3N_4/TiO_2 nanocomposite and it confirms the Ti, O, C and N elements presence. Figure 6b of Ti 2p core-level spectrum has two peaks at 458 and 464 eV reveals that the TiO_2 is present as Ti(IV) state in the g-C_3N_4/TiO_2 nanocomposite. Figure 6c shows the O 1 s core level spectrum, in which, the peaks at 528 and 530 eV corresponds to binding energies of O atom in TiO_2 and atmospheric oxygen [51]. Figure 6d shows core level spectrum of C 1 s, in which, binding energy values centered at around 283, 285 and 286 eV are observed. The peak at 283 eV is typically ascribed to the sp^2 C=C bonds, the peak at 285 eV can be assigned to the sp^2-hybridized carbon atom bonded to three nitrogen atoms in the g-C_3N_4 layer and the peak at 286 eV can be attributed to the sp^2 carbon atoms in the aromatic ring attached to the –NH_2 group [52, 53].

Figure 6e shows core level spectrum of N 1 s, in which, three peaks were absorbed at 395, 397 and 399 eV. The peak at 395 eV is attributed to sp^2-hybridized nitrogen (C–N–C), the peak at 397 eV is contributed to sp^3-tertiary nitrogen (N–[C]$_3$) and the peak at 399 eV is assigned to the sp^3-tertiary nitrogen (N–[C]$_3$) and NHx groups, which are typical to the heptazine units of g-C_3N_4 [54].

3.6 Thermogravimetric analysis

Thermogravimetric analysis of g-C_3N_4/TiO_2 nanocomposite was performed from room temperature to 800 °C in nitrogen atmosphere to measure the weight loss because of the decomposition of g-C_3N_4. Figure 5b shows TGA of the g-C_3N_4, TiO_2 and 20% g-C_3N_4/TiO_2 under nitrogen

atmosphere from room temperature to 800 °C at a heating rate of 10 °C min^{-1}. TiO_2 does not show any weight loss while pure g-C_3N_4 completely decomposes when the temperature exceeds 740 °C. For nanocomposite, g-C_3N_4 starts to decompose around 440 °C and could be totally removed when it reaches 630 °C. This is because of the weaker thermal stability of g-C_3N_4 in g-C_3N_4/TiO_2 nanocomposite than that of pure g-C_3N_4 [51]. From the Fig. 5b, the calculated wt.% of the g-C_3N_4 content in the 20% g-C_3N_4/TiO_2 nanocomposite is found to be 18.2.

3.7 Morphological studies

The morphological features were examined using HRTEM images of the samples. Figure 7a–c shows the HRTEM images of 10% g-C_3N_4/TiO_2. From Fig. 7a–c, it is clearly seen the formation of g-C_3N_4 nanoplatelets incorporated TiO_2 nanostructures. Also, the formation of heterostructure in-between g-C_3N_4 and TiO_2 was clearly observed. Figure 7d, e shows the lattice fringes of 10% g-C_3N_4/TiO_2 nanocomposites. The 'd' values calculated from the XRD pattern clearly matches with 'd' values obtained from the lattice fringes. Figure 7f shows the selected area electron diffraction (SAED) pattern of g-C_3N_4/TiO_2 nanocomposites reveals the polycrystalline nature.

3.8 Photoelectrocatalytic water splitting studies

The role of g-C_3N_4 on TiO_2 towards photoelectrocatalytic water splitting was investigated by recording linear sweep voltammogram (LSV) under simulated illumination of 100 mW cm^{-2} (AM 1.5 G) in 1 M KOH (pH = 13.2). Figure 8a displays LSV curves of g-C_3N_4, TiO_2
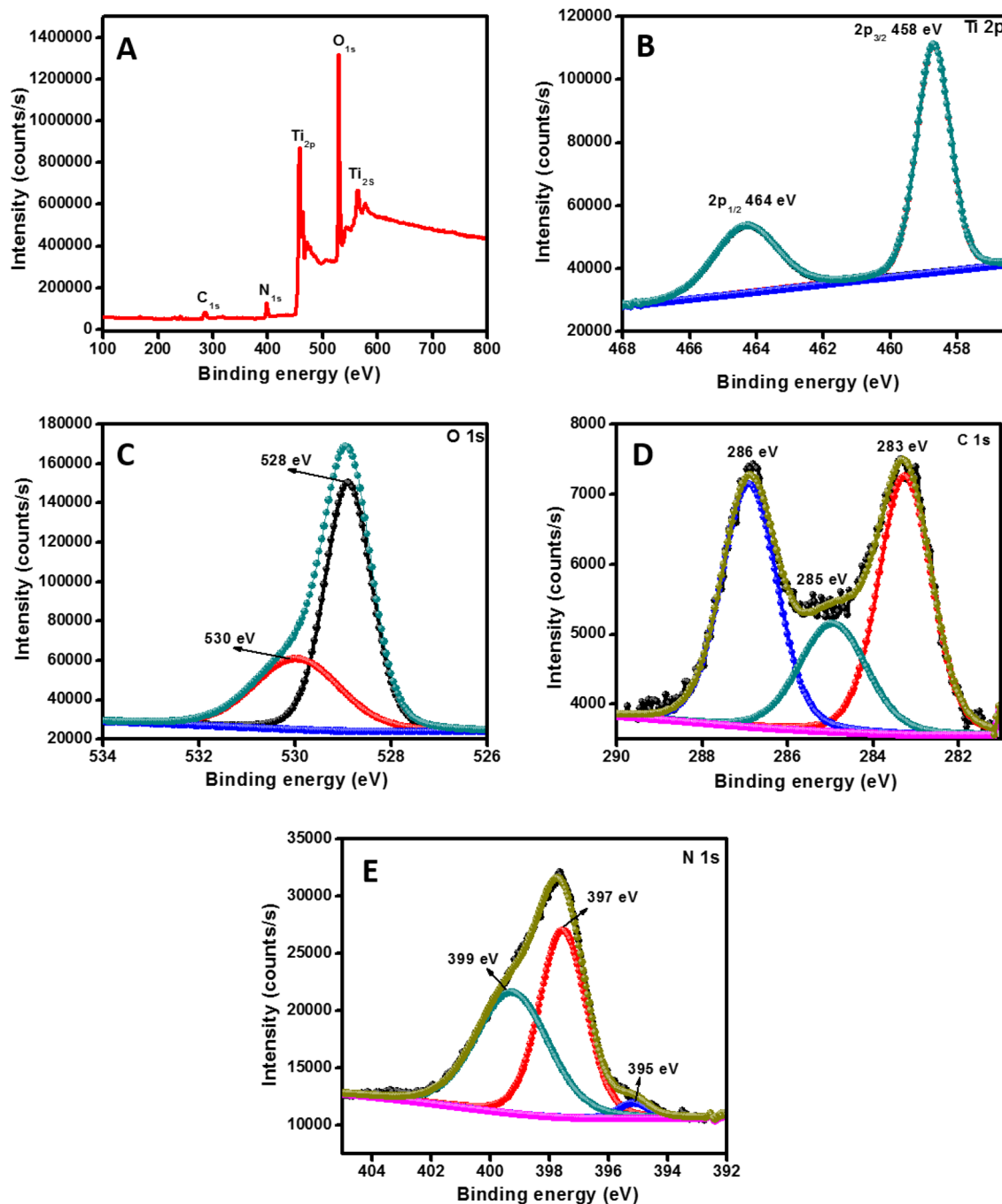
Fig. 6 XPS spectra of g-C_3N_4/TiO_2 nanocomposite and its corresponding **a** survey scan, **b** Ti 2p, **c** O 1s, **d** C 1s and **e** N 1s core-level spectra

and g-C_3N_4/TiO_2 composite material under illumination, which clearly shows the bare g-C_3N_4 have negligible photocurrent response attributed to the high recombination of photogenerated charge carriers and the g-C_3N_4/TiO_2 composite shows better PEC activity than bare TiO_2. The photocurrent density of photoanode fabricated by g-C_3N_4/TiO_2 composite is 142.7 μA cm^{-2} (at 1.23 V vs. RHE) which is ∼ 1.8-fold higher than bare TiO_2

(80.5 μA cm^{-2} at 1.23 V vs. RHE). The enhancement of PEC activity in g-C_3N_4/TiO_2 composite due to the formation of heterostructure in-between g-C_3N_4 and TiO_2, it reduces the rate of recombination of photo-generated electron–hole pairs [41, 55]. Moreover, the formation of heterostructure effectively increases the absorption of TiO_2 to visible light range and boost up the interfacial charge transfer between electrode/electrolyte interfaces,

Fig. 7 **a**, **b**, **c** and **d** HRTEM images of 10% g-C$_3$N$_4$/TiO$_2$, **d** and **e** Lattice resolved HRTM image of 10% g-C$_3$N$_4$/TiO$_2$ and **f** SAED pattern of 10% g-C$_3$N$_4$/TiO$_2$
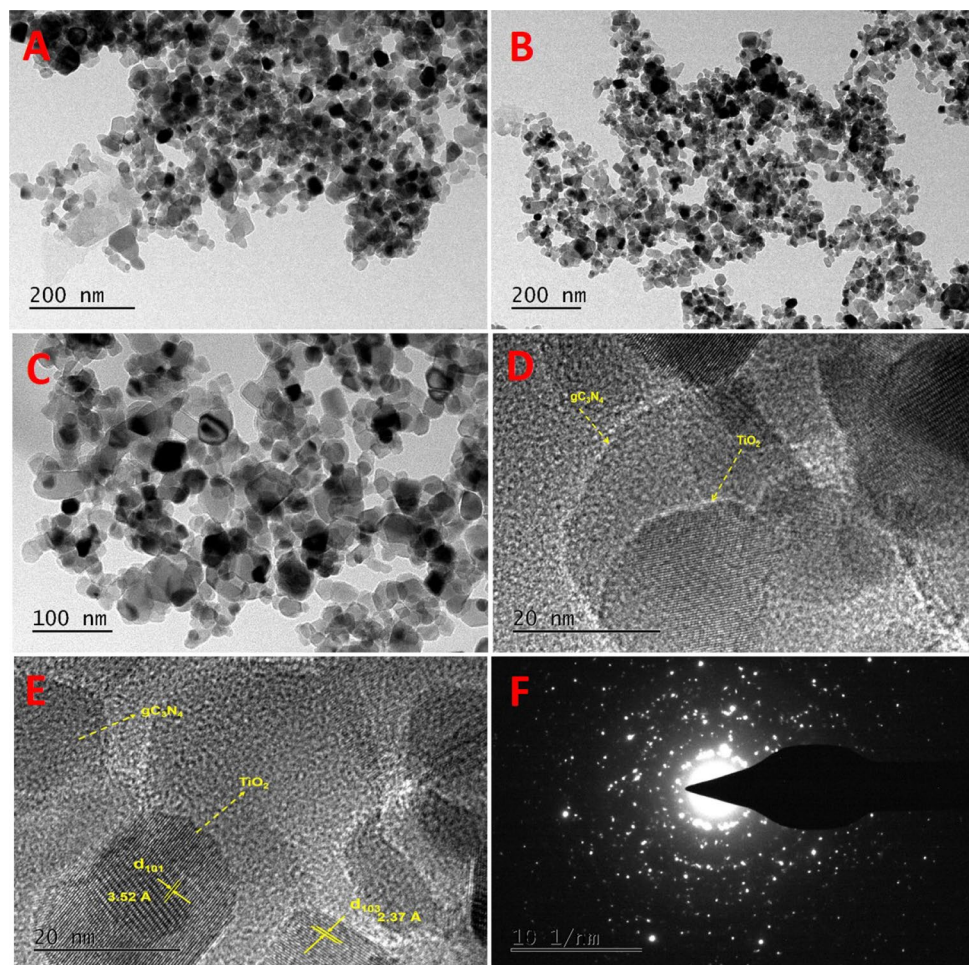
which enhance the PEC perfomance of the g-C$_3$N$_4$/TiO$_2$ composite.

Figure 8b, c shows the sudden rise and fall in the photocurrent in both LSV and J-T curves, which indicates the quick photo-response of the TiO$_2$ and g-C$_3$N$_4$/TiO$_2$ photoanode under the light and dark condition. The J–T curve shows a constant increase and decrease in the photocurrent under light and dark condition, it clearly indicates the excellent photochemical stability of the electrode fabricated by g-C$_3$N$_4$/TiO$_2$ composite.

The efficiency of the TiO$_2$ and g-C$_3$N$_4$/TiO$_2$ composite photoanodes was further evaluated through solar to hydrogen (STH) efficiency (η) can be calculated following the equation.

$$\eta(\%) = \frac{J_p \times (1.23 - V)}{P_{light}} \times 100 \qquad (3)$$

Here Jp is the photocurrent density (mA cm^{-2}), P$_{light}$ is the incident light power density (mW cm^{-2}) and V is the voltage applied versus RHE [56, 57]. Figure 8d shows the plot of STH efficiency against applied potential (vs. RHE), which

is good acceptance with LSV results. The g-C$_3$N$_4$/TiO$_2$ photoanode achieves a maximum efficiency of ~0.072%, which is 2- fold higher than bare TiO$_2$ (0.035%).

Further, the charge transfer property of TiO$_2$ and g-C$_3$N$_4$/TiO$_2$ photoanodes was studied by using electrochemical impedance spectroscopy (EIS) technique. Figure 8e displays the Nyquist plots of TiO$_2$ and g-C$_3$N$_4$/TiO$_2$, from that the g-C$_3$N$_4$/TiO$_2$ photoanode show smallest semicircle radii compare to TiO$_2$, which means the g-C$_3$N$_4$/TiO$_2$ photoanode having smallest electron transfer resistance, highest electrical conductivity, and rapid charge transfer across the electrode/electrolyte interface, which reduces the rate of electron–hole pair recombination and enhance the PEC activity of the g-C$_3$N$_4$/TiO$_2$ composite [41, 58].

The charge migration direction in the heterostructure was explain by band-edge potential level calculation of semiconductors. The determined band-gap values for TiO$_2$ and g-C$_3$N$_4$ were 3.1 and 2.75 eV, respectively. The conduction and valence band positions of the prepared samples were calculated by the Eq. (4) and (5)
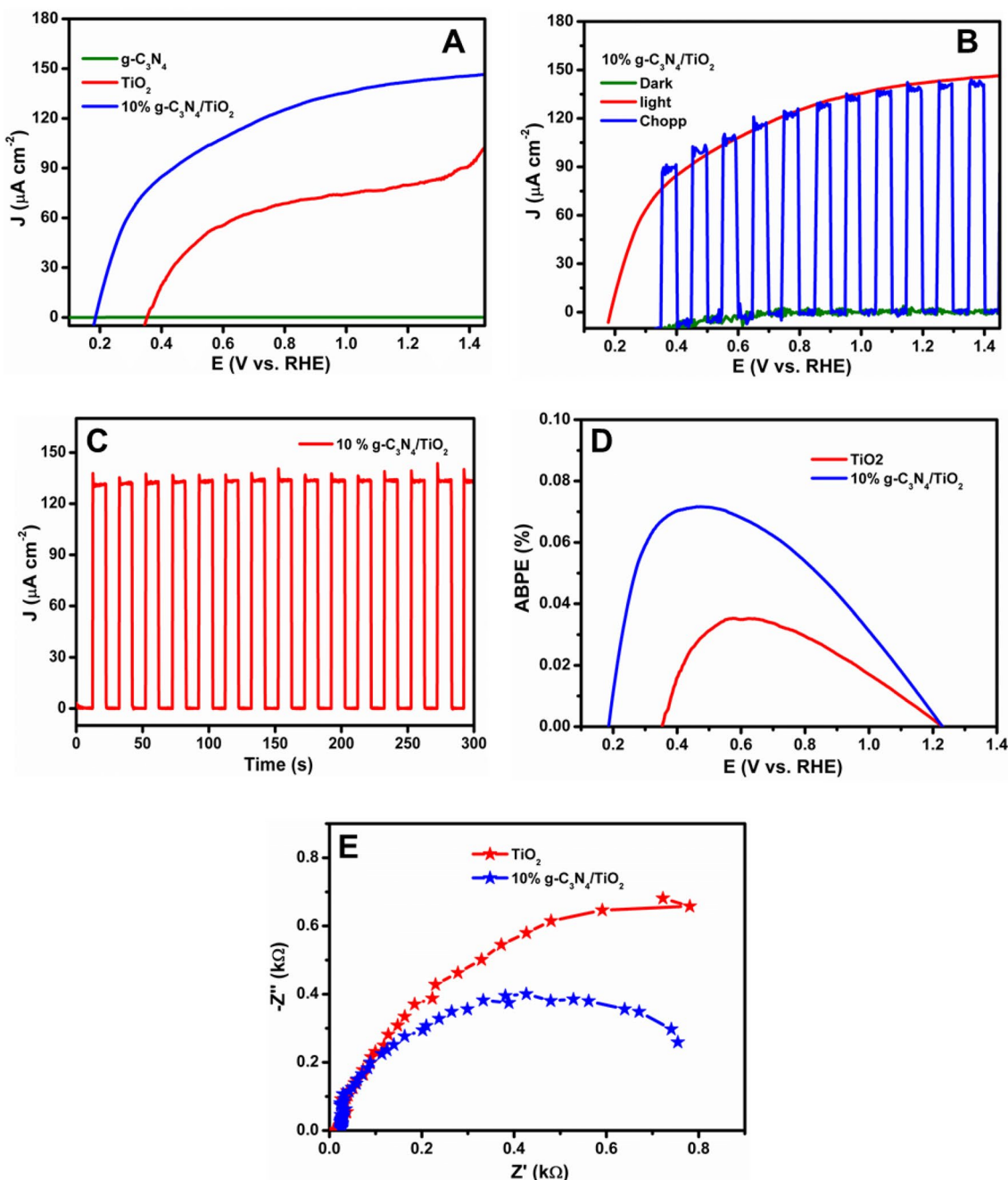
Fig. 8 **a** Linear sweep voltammograms obtained for g-C$_3$N$_4$, TiO$_2$ and g-C$_3$N$_4$/TiO$_2$- composite modified photoanode under light illumination of 100 mW cm^{-2} (AM 1.5G) at a scan rate of 10 mV/s in 1 M KOH. **b** Linear sweep voltammograms of g-C$_3$N$_4$/TiO$_2$- under dark, light and chopped illumination condition. **c** Chronoamperometric J–T curve obtained for g-C$_3$N$_4$/TiO$_2$- at 1.23 V versus RHE in 1 M KOH. **d** Plot of STH (η) (%) versus applied potential obtained for TiO$_2$ and g-C$_3$N$_4$/TiO$_2$. **e** EIS Nyquist plots obtained for TiO$_2$ and 10%-g-C$_3$N$_4$/TiO$_2$ under light illumination of 100 mW cm^{-2} (AM 1.5 G) at an amplitude of 10 mV and frequency range of 100 mHz–100 kHz in 1 M KOH

$$E_{VB} = \chi - E^e + 0.5E_g \qquad (4)$$

$$E_{CB} = E_{VB} - E_g \qquad (5)$$

where χ is Mulliken's electronegativity, E^e is the energy of free electrons on the hydrogen scale (4.50 eV) and E_g is the band gap [59, 60]. The absolute electronegativity of pure TiO$_2$ and g-C$_3$N$_4$ is 5.81 and 4.64 eV, respectively [61, 62]. The calculated valance band (VB) of g-C$_3$N$_4$ and TiO$_2$ is

+1.515 and +2.86 eV, respectively. Whereas, the conduction band (CB) of g-C_3N_4 and TiO_2 is −1.235 and −0.24 eV, respectively.

The CB of g-C_3N_4 is more negative than CB of TiO_2, its leads to easily transfer of the photogenerated electron from CB of g-C_3N_4 to CB of TiO_2 via heterostructure in-between TiO_2 and g-C_3N_4 interface. On the other hand, the photogenerated holes are transferred from the VB of TiO_2 (+2.86 eV) to the VB of g-C_3N_4 (+1.515). That leads to formation of Type-II heterostructure between TiO_2 and g-C_3N_4 interface [48, 63, 64]. Moreover, the VB of the g-C_3N_4 and TiO_2 was calculated from XPS valence band

analysis, Fig. 9 shows the XPS valence band spectra of g-C_3N_4 and TiO_2, from that the VB of g-C_3N_4 and TiO_2 are +1.45 and +2.72 eV, respectively. Therefore, the CB of TiO_2 and g-C_3N_4 are -0.38 and −1.30 eV, respectively. It is almost similar to values calculated from equation. Based on the calculation, XPS valence band analysis and previous reports, the CB edge potential of g-C_3N_4 (−1.30 eV) is much more negative, while compared to the CB of TiO_2 (−0.38 eV), which leads to easy transfer of photogenerated electron from the CB of g-C_3N_4 to the CB of TiO_2. Similarly, the photogenerated holes are transferred from the VB of TiO_2 (+2.72 eV) to the VB of g-C_3N_4 (+1.45 eV) [21, 43, 50,

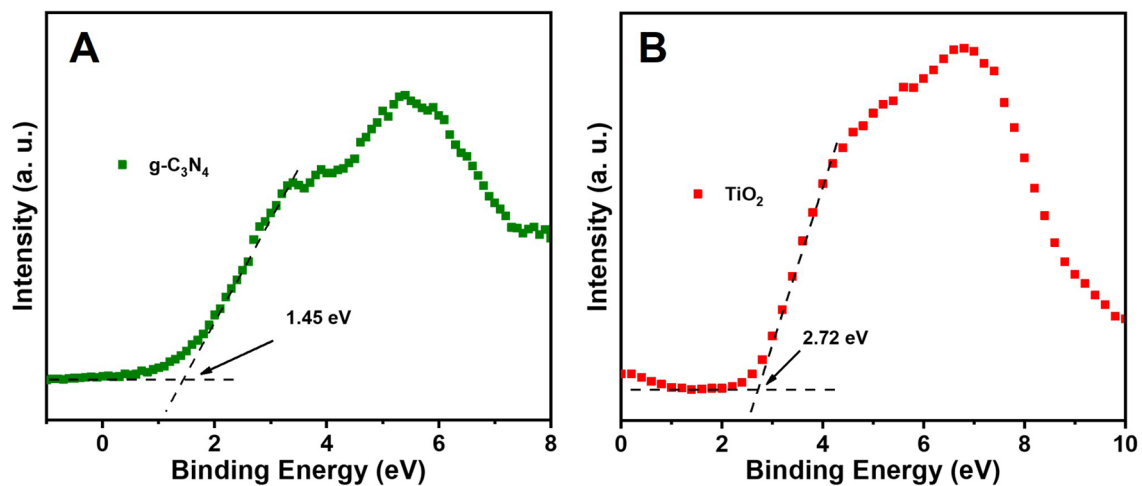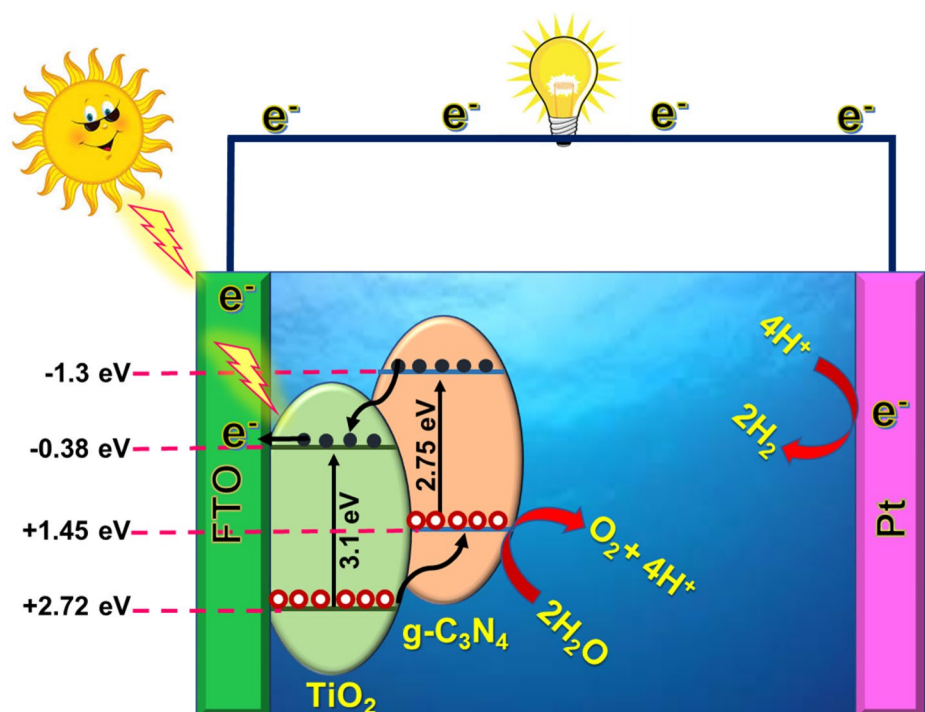**Fig. 9** XPS Valence band spectra of **a** g-C_3N_4 and **b** TiO_2

Fig. 10 Schematic of overall photoelectrocatalytic water splitting mechanism in the g-C_3N_4@TiO_2 photoanode based on Type-II heterostructure

58]. From the result, the incorporation of g-C_3N_4 to TiO_2 leads to formation Type-II heterostructure (Fig. 10), which reduced the rate of recombination of photo-generated electron–hole pairs, effectively extends the absorption of TiO_2 to visible light range and enhance the interfacial charge transfer between electrode/electrolyte interfaces.

4 Conclusion

In overview, the g-C_3N_4/TiO_2 nanoplatelets materials with different weight percentage of g-C_3N_4 were prepared. The prepared nanocomposite showed an excellent optical absorption and improved PEC performance. The g-C_3N_4/TiO_2 nanohybrid showed enhanced PEC performance than bare TiO_2 and g-C_3N_4-, due to fast interfacial charge transfer and slow recombination rate of electron hole pairs. The g-C_3N_4/TiO_2 photoanode yields a maximum efficiency of ~ 0.072%, which is twofold higher than bare TiO_2 (0.035%), due to the formation of Type-II heterostructure in-between g-C_3N_4 nanoplatelets and TiO_2, that leads to the reduction of the recombination rate of photo-generated electron–hole pairs and also increases the absorption of TiO_2 to visible light range and boost up the interfacial charge transfer between electrode/electrolyte interface, which enhance the PEC performance of the g-C_3N_4/TiO_2 composite. The results indicate that the g-C_3N_4/TiO_2 nanocomposite material could be a potential candidate for photoelectrocatalytic hydrogen production via water splitting.

Compliance with ethical standards

Conflict of interest The authors declare that they have no conflict of interest.

References

1. Davis SJ, Caldeira K (2010) Consumption-based accounting of CO_2 emissions. Proc Natl Acad Sci 107:5687–5692. https://doi.org/10.1073/pnas.0906974107
2. Dodman D (2009) Blaming cities for climate change? An analysis of urban greenhouse gas emissions inventories. Environ Urban 21:185–201. https://doi.org/10.1177/0956247809103016
3. Fujishima A, Honda K (1972) Electrochemical photolysis of water at a semiconductor electrode. Nature 238:37–38. https://doi.org/10.1038/238037a0
4. Ozawa H, Sakai K (2011) Photo-hydrogen-evolving molecular devices driving visible-light-induced water reduction into molecular hydrogen: structure–activity relationship and reaction mechanism. Chem Commun 47:2227. https://doi.org/10.1039/c0cc04708b
5. Zhu M, Chen P, Liu M (2011) Graphene oxide enwrapped Ag/AgX (X = Br, Cl) nanocomposite as a highly efficient visible-light plasmonic photocatalyst. ACS Nano 5:4529–4536. https://doi.org/10.1021/nn200088x
6. Walter MG, Warren EL, Mc Kone JR, Boettcher SW, Mi Q, Santori EA, Lewis NS (2010) Solar water splitting cells. Chem Rev 110:6446–6473. https://doi.org/10.1021/cr1002326
7. Ma Y, Wang X, Jia Y, Chen X, Han H, Li C (2014) Titanium dioxide-based nanomaterials for photocatalytic fuel generations. Chem Rev 114:9987–10043. https://doi.org/10.1021/cr500008u
8. Barber J (2009) Photosynthetic energy conversion: natural and artificial. Chem Soc Rev 38:185–196. https://doi.org/10.1039/B802262N
9. Tachibana Y, Vayssieres L, Durrant JR (2012) Artificial photosynthesis for solar water-splitting. Nat Photonics 6:511–518. https://doi.org/10.1038/nphoton.2012.175
10. Lewis NS, Nocera DG (2006) Powering the planet: chemical challenges in solar energy utilization. Proc Natl Acad Sci 103:15729–15735. https://doi.org/10.1073/pnas.0603395103
11. Lee WJ, Shinde PS, Go GH, Ramasamy E (2011) Ag grid induced photocurrent enhancement in WO_3 photoanodes and their scale-up performance toward photoelectrochemical H_2 generation. Int J Hydrog Energy 36:5262–5270. https://doi.org/10.1016/j.ijhydene.2011.02.013
12. Bak T, Nowotny J, Rekas M, Sorrell C (2002) Photo-electrochemical hydrogen generation from water using solar energy. Materials-related aspects. Int J Hydrog Energy 27:991–1022. https://doi.org/10.1016/S0360-3199(02)00022-8
13. Ong WJ, Tan LL, Chai SP, Yong ST, Mohamed AR (2014) Self-assembly of nitrogen-doped TiO_2 with exposed 001 facets on a graphene scaffold as photo-active hybrid nanostructures for reduction of carbon dioxide to methane. Nano Res 7:1528–1547. https://doi.org/10.1007/s12274-014-0514-z
14. Ong WJ, Tan LL, Chai SP, Yong ST, Mohamed AR (2014) Facet-dependent photocatalytic properties of TiO_2-based composites for energy conversion and environmental remediation. Chemsuschem 7:690–719. https://doi.org/10.1002/cssc.201300924
15. Yu P, Zhang J (2015) Some interesting properties of black hydrogen-treated TiO_2 nanowires and their potential application in solar energy conversion. Sci China Chem 58:1810–1815. https://doi.org/10.1007/s11426-015-5400-3
16. Wang J, Sun H, Huang J, Li Q, Yang J (2014) Band structure tuning of TiO_2 for enhanced photoelectrochemical water splitting. J Phys Chem C 118:7451–7457. https://doi.org/10.1021/jp5004775
17. Chen X, Burda C (2008) The electronic origin of the visible-light absorption properties of C-, N- and S-Doped TiO_2 nanomaterials. J Am Chem Soc 130:5018–5019. https://doi.org/10.1021/ja711023z
18. Tatsuma T, Saitoh S, Ohko Y, Fujishima A (2001) $TiO_2 - WO_3$ photoelectrochemical anticorrosion system with an energy storage ability. Chem Mater 13:2838–2842. https://doi.org/10.1021/cm010024k
19. Formo E, Lee E, Campbell D, Xia Y (2008) Functionalization of electrospun TiO_2 nanofibers with Pt nanoparticles and nanowires for catalytic applications. Nano Lett 8:668–672. https://doi.org/10.1021/nl073163v

20. Williams G, Seger B, Kamat PV (2008) TiO_2-graphene nanocomposites. UV-assisted photocatalytic reduction of graphene oxide. ACS Nano. 2:1487–1491. https://doi.org/10.1021/nn800251f

21. Bao Y, Chen K (2016) AgCl/Ag/g-C_3N_4 hybrid composites: preparation, visible light-driven photocatalytic activity and mechanism. Nano-Micro Lett 8:182–192. https://doi.org/10.1007/s40820-015-0076-y

22. Liang Q, Jin J, Zhang M, Liu C, Xu S, Yao C, Li Z (2017) Construction of mesoporous carbon nitride/binary metal sulfide heterojunction photocatalysts for enhanced degradation of pollution under visible light. Appl Catal B Environ 218:545–554. https://doi.org/10.1016/j.apcatb.2017.07.003

23. Hou Y, Wen Z, Cui S, Guo X, Chen J (2013) Constructing 2D porous graphitic C_3N_4 nanosheets/nitrogen-doped graphene/layered MoS2 ternary nanojunction with enhanced photoelectrochemical activity. Adv Mater 25:6291–6297. https://doi.org/10.1002/adma.201303116

24. Zhang Y, Mori T, Ye J, Antonietti M (2010) Phosphorus-doped carbon nitride solid: enhanced electrical conductivity and photocurrent generation. J Am Chem Soc 132:6294–6295. https://doi.org/10.1021/ja101749y

25. Wang X, Maeda K, Chen X, Takanabe K, Domen K, Hou Y, Fu X, Antonietti M (2009) Polymer semiconductors for artificial photosynthesis: hydrogen evolution by mesoporous graphitic carbon nitride with visible light. J Am Chem Soc 131:1680–1681. https://doi.org/10.1021/ja809307s

26. Liao G, Chen S, Quan X, Yu H, Zhao H (2012) Graphene oxide modified g-C_3N_4 hybrid with enhanced photocatalytic capability under visible light irradiation. J Mater Chem 22:2721–2726. https://doi.org/10.1039/C1JM13490F

27. Wang WW, Zhu YJ, Yang LX (2007) ZnO–SnO_2 hollow spheres and hierarchical nanosheets: hydrothermal preparation, formation mechanism, and photocatalytic properties. Adv Funct Mater 17:59–64. https://doi.org/10.1002/adfm.200600431

28. Xu TG, Zhang C, Shao X, Wu K, Zhu YF (2006) Monomolecular-layer $Ba_5Ta_4O_{15}$ nanosheets: synthesis and investigation of photocatalytic properties. Adv Funct Mater 16:1599–1607. https://doi.org/10.1002/adfm.200500849

29. Zhang C, Zhu Y (2005) Synthesis of square Bi_2WO_6 nanoplates as high-activity visible-light-driven photocatalysts. Chem Mater 17:3537–3545. https://doi.org/10.1021/cm0501517

30. Cheng F, Yan J, Zhou C, Chen B, Li P, Chen Z, Dong X (2016) An alkali treating strategy for the colloidization of graphitic carbon nitride and its excellent photocatalytic performance. J Colloid Interface Sci 468:103–109. https://doi.org/10.1016/j.jcis.2016.01.044

31. Yan J, Han X, Qian J, Liu J, Dong X, Xi F (2017) Preparation of 2D graphitic carbon nitride nanosheets by a green exfoliation approach and the enhanced photocatalytic performance. J Mater Sci 52:13091–13102. https://doi.org/10.1007/s10853-017-1419-5

32. Niu P, Zhang L, Liu G, Cheng HM (2012) Graphene-like carbon nitride nanosheets for improved photocatalytic activities. Adv Funct Mater 22:4763–4770. https://doi.org/10.1002/adfm.201200922

33. Yang S, Gong Y, Zhang J, Zhan L, Ma L, Fang Z, Vajtai R, Wang X, Ajayan PM (2013) Exfoliated graphitic carbon nitride nanosheets as efficient catalysts for hydrogen evolution under visible light. Adv Mater 25:2452–2456. https://doi.org/10.1002/adma.201204453

34. Zhang X, Xie X, Wang H, Zhang J, Pan B, Xie Y (2013) Enhanced photoresponsive ultrathin graphitic-phase C_3N_4 nanosheets for bioimaging. J Am Chem Soc 135:18–21. https://doi.org/10.1021/ja308249k

35. Qian J, Yan J, Shen C, Xi F, Dong X, Liu J (2018) Graphene quantum dots-assisted exfoliation of graphitic carbon nitride to prepare metal-free zero-dimensional/two-dimensional composite photocatalysts. J Mater Sci 53:12103–12114. https://doi.org/10.1007/s10853-018-2509-8

36. Cheng F, Wanga H, Donga X (2013) The amphoteric property of g-C_3N_4 nanosheets and its relevant heterostructure photocatalysts by an electrostatic re-assembly route. Chem Commun 135:18–21. https://doi.org/10.1039/b000000x

37. Han Q, Zhao F, Hu C, Lv L, Zhang Z, Chen N, Qu L (2015) Facile production of ultrathin graphitic carbon nitride nanoplatelets for efficient visible-light water splitting. Nano Res 8:1718–1728. https://doi.org/10.1007/s12274-014-0675-9

38. Yan J, Zhou C, Li P, Chen B, Zhang S, Dong X, Xi F, Liu J (2016) Nitrogen-rich graphitic carbon nitride: controllable nanosheet-like morphology, enhanced visible light absorption and superior photocatalytic performance. Colloids Surf A Physicochem Eng Asp 508:257–264. https://doi.org/10.1016/j.colsurfa.2016.08.067

39. Han X, Yuan A, Yao C, Xi F, Liu J, Dong X (2019) Synergistic effects of phosphorous/sulfur co-doping and morphological regulation for enhanced photocatalytic performance of graphitic carbon nitride nanosheets. J Mater Sci 54:1593–1605. https://doi.org/10.1007/s10853-018-2925-9

40. Qian J, Yuan A, Yao C, Liu J, Li B, Xi F, Dong X (2018) Highly efficient photo-reduction of p-nitrophenol by protonated graphitic carbon nitride nanosheets. ChemCatChem 10:4747–4754. https://doi.org/10.1002/cctc.201801146

41. Wei Q, Yan X, Kang Z, Zhang Z, Cao S, Liu Y, Zhang Y (2017) Carbon quantum dots decorated C_3N_4/TiO_2 heterostructure nanorod arrays for enhanced photoelectrochemical performance. J Electrochem Soc 164:H515–H520. https://doi.org/10.1149/2.1281707jes

42. Troppová M, Šihor M, Reli M, Ritz P, Praus K Kočí (2018) Unconventionally prepared g-C_3N_4/TiO_2 photocatalysts for photocatalytic decomposition of nitrous oxide. Appl Surf Sci 430:335–347. https://doi.org/10.1016/j.apsusc.2017.06.299

43. Jiang Z, Zhu C, Wan W, Qian K, Xie J (2016) Constructing graphite-like carbon nitride modified hierarchical yolk–shell TiO_2 spheres for water pollution treatment and hydrogen production. J Mater Chem A 4:1806–1818. https://doi.org/10.1039/C5TA09919F

44. Li J, Zhang M, Li Q, Yang J (2017) Enhanced visible light activity on direct contact Z-scheme g-C_3N_4-TiO_2 photocatalyst. Appl Surf Sci 391:184–193. https://doi.org/10.1016/j.apsusc.2016.06.145

45. Zang Y, Li L, Xu Y, Zuo Y, Li G (2014) Hybridization of brookite TiO_2 with g-C_3N_4: a visible-light-driven photocatalyst for As^{3+} oxidation, MO degradation and water splitting for hydrogen evolution. J Mater Chem A 2:15774–15780. https://doi.org/10.1039/c4ta02082k

46. Joshi MM, Labhsetwar NK, Mangrulkar PA, Tijare SN, Kamble SP, Rayalu SS (2009) Visible light induced photoreduction of methyl orange by N-doped mesoporous titania. Appl Catal A Gen 357:26–33. https://doi.org/10.1016/j.apcata.2008.12.030

47. Wei Z, Liang F, Liu Y, Luo W, Wang J, Yao W, Zhu Y (2017) Photoelectrocatalytic degradation of phenol-containing wastewater by TiO_2/g-C_3N_4 hybrid heterostructure thin film. Appl Catal B Environ 201:600–606. https://doi.org/10.1016/j.apcatb.2016.09.003

48. Senthil RA, Theerthagiri J, Selvi A, Madhavan J (2017) Synthesis and characterization of low-cost g-C_3N_4/TiO_2 composite with enhanced photocatalytic performance under visible-light irradiation. Opt Mater (Amst) 64:533–539. https://doi.org/10.1016/j.optmat.2017.01.025

49. Li J, Liu Y, Li H, Chen C (2016) Fabrication of g-C_3N_4/TiO_2 composite photocatalyst with extended absorption wavelength range and enhanced photocatalytic performance. J Photochem

Photobiol A Chem 317:151–160. https://doi.org/10.1016/j.jphotochem.2015.11.008

50. Wang M, Liu Z, Fang M, Tang C, Huang Z, Liu Y, Wu X, Mao Y (2016) Enhancement in the photocatalytic activity of TiO_2 nanofibers hybridized with g-C_3N_4 via electrospinning. Solid State Sci 55:1–7. https://doi.org/10.1016/j.solidstatesciences.2016.02.002

51. Tong Z, Yang D, Xiao T, Tian Y, Jiang Z (2015) Biomimetic fabrication of g-C_3N_4/TiO_2 nanosheets with enhanced photocatalytic activity toward organic pollutant degradation. Chem Eng J 260:117–125. https://doi.org/10.1016/j.cej.2014.08.072

52. Yao C, Wang R, Wang Z, Lei H, Dong X, He C (2019) Highly dispersive and stable Fe^{3+} active sites on 2D graphitic carbon nitride nanosheets for efficient visible-light photocatalytic nitrogen fixation. J Mater Chem A 7:27547–27559. https://doi.org/10.1039/c9ta09201c

53. Yao C, Yuan A, Wang Z, Lei H, Zhang L, Guo L, Dong X (2019) Amphiphilic two-dimensional graphitic carbon nitride nanosheets for visible-light-driven phase-boundary photocatalysis. J Mater Chem A 7:13071–13079. https://doi.org/10.1039/c9ta03253c

54. Yuan A, Lei H, Wang Z, Dong X (2020) Improved photocatalytic performance for selective oxidation of amines to imines on graphitic carbon nitride/bismuth tungstate heterojunctions. J Colloid Interface Sci 560:40–49. https://doi.org/10.1016/j.jcis.2019.10.060

55. Liu P, Huo X, Tang Y, Xu J, Liu X, Wong DKY (2017) A TiO_2 nanosheet-g-C_3N_4 composite photoelectrochemical enzyme biosensor excitable by visible irradiation. Anal Chim Acta 984:86–95. https://doi.org/10.1016/j.aca.2017.06.043

56. Zhang X, Zhang B, Cao K, Brillet J, Chen J, Wang M, Shen Y (2015) A perovskite solar cell-TiO_2@$BiVO_4$ photoelectrochemical system for direct solar water splitting. J Mater Chem A 3:21630–21636. https://doi.org/10.1039/C5TA05838D

57. Dotan H, Mathews N, Hisatomi T, Grätzel M, Rothschild A (2014) On the solar to hydrogen conversion efficiency of photoelectrodes for water splitting. J. Phys. Chem. Lett. 5:3330–3334. https://doi.org/10.1021/jz501716g

58. Murugan C, Abinav Nataraj R, Praveen Kumar M, Ravichandran S, Pandikumar A (2019) Enhanced charge transfer process of bismuth vanadate interleaved graphitic carbon nitride nanohybrids in mediator-free direct Z scheme photoelectrocatalytic water splitting. ChemistrySelect 4:4653–4663. https://doi.org/10.1002/slct.201900732

59. Yu C, Li G, Kumar S, Kawasaki H, Jin R (2013) Stable Au 25 (SR)$_{18}$/TiO_2 composite nanostructure with enhanced visible light photocatalytic activity. J Phys Chem Lett 4:2847–2852. https://doi.org/10.1021/jz401447w

60. Wang J, Guo P, Dou M, Wang J, Cheng Y, Jönsson PG, Zhao Z (2014) Visible light-driven g-C_3N_4/m-$Ag_2Mo_2O_7$ composite photocatalysts: synthesis, enhanced activity and photocatalytic mechanism. RSC Adv 4:51008–51015. https://doi.org/10.1039/C4RA09224D

61. Lu H, Fan W, Dong H, Liu L (2017) Dependence of the irradiation conditions and crystalline phases of TiO_2 nanoparticles on their toxicity to Daphnia magna. Environ Sci Nano 4:406–414. https://doi.org/10.1039/C6EN00391E

62. Leong KH, Tan ZZ, Sim LC, Saravanan P, Bahnemann D, Jang M (2017) Symbiotic interaction of amalgamated photocatalysts with improved day light utilisation and charge separation. ChemistrySelect 2:84–89. https://doi.org/10.1002/slct.201601490

63. Rameshbabu R, Ravi P, Sathish M (2019) Cauliflower-like CuS/ZnS nanocomposites decorated g-C_3N_4 nanosheets as noble metal-free photocatalyst for superior photocatalytic water splitting. Chem Eng J 360:1277–1286. https://doi.org/10.1016/j.cej.2018.10.180

64. Liu H, Zhang ZG, He HW, Wang XX, Zhang J, Zhang QQ, Tong YF, Liu HL, Ramakrishna S, Yan SY, Long YZ (2018) One-step synthesis heterostructured g-C_3N_4/TiO_2 composite for rapid degradation of pollutants in utilizing visible light. Nanomaterials 8:842. https://doi.org/10.3390/nano8100842